# Comparison of the Flow Field of a Swirl Stabilized Premixed Burner in an Annular and a Single Burner Combustion Chamber

**D. Fanaca**

**P. R. Alemela**

**C. Hirsch**
e-mail: hirsch@td.mw.tum.de

**T. Sattelmayer**

Lehrstuhl für Thermodynamik,
TU München,
85748 Garching, Germany

*An experimental investigation of the flow field of a 12 burner annular combustor and a single burner combustor with the same burner was performed. It has revealed the aerodynamic effect, which causes the discrepancies in the flame transfer function behavior measured at the same operating conditions in the single and the annular combustion chambers. The results have shown significant differences in the flow field. In particular, it is seen that for the investigated system in the annular combustor a free swirling jet flow forms, while in the single burner configuration, a swirling wall jet flow regime exists. In this paper, we discuss the physical mechanism and show how to generalize an earlier finding, which identified a critical confinement value for a given swirler. We propose a new correlation for coswirling burners, which explains the changes found for the investigated system. It compares also well with the experimental data from other burner geometries. The correlation should allow to design single burner tests as to match the annular combustor flow regime.* [DOI: 10.1115/1.4000120]

## 1 Introduction

The stability of lean premixed combustion systems with regard to self-sustained combustion instabilities can be evaluated with a stability analysis using the acoustic network modeling approach [1–4]. It requires the knowledge of the dynamic behavior of the flame in terms of the acoustical transfer matrices or transfer functions. Because of their complexity, often these functions are measured [5] or derived from more complex models, which are based on experimental investigations.

The fundamental method to obtain the flame transfer matrix was proposed in Refs. [6,7]. Due to cost effectiveness and experimental feasibility, the experimental determination of the dynamic flame characteristics is often performed in single burner configurations (SCCs) [8–10] and the data are then used to perform the stability analysis on multiburner combustor systems, e.g., annular combustors (ACCs). In doing so, close similarity of the flame in both systems is assumed. While some success has been achieved with this procedure, the underlying assumption has never been qualified. Therefore, a comprehensive experimental and theoretical study was conducted at the Lehrstuhl für Thermodynamik of TU München with the Alstom EV5 model burner on both a 12 burner annular and its corresponding single burner combustor. In previous papers [11,12], the detailed results of the study on flame dynamics in both systems, as well as the method of analysis, have been reported. It was found that the flame transfer functions measured for the EV5 burner in the single and the annular combustor at the same operating conditions are different. There it was shown that the flames could be well described by the following parametrized flame transfer function, Eq. (1), proposed by Schuermans et al. [13]:

$$\mathrm{FTF} \equiv \frac{\dot{Q}'/\bar{\dot{Q}}}{u'/\bar{u}} = n\,\exp(-i\omega\tau)\cdot\exp\left(-\frac{1}{2}\omega^2\sigma^2\right) \tag{1}$$

As an example for the difference between annular and single combustor characteristics, the parameters for an externally premixed flame are given in Table 1. The presented data have been normalized with the nominal burner diameter $d_0$ and the nominal velocity $u_0$ in the following way:

$$\tau^* = \frac{u_0\cdot\tau}{d_0}, \quad \sigma^* = \frac{u_0\cdot\sigma}{d_0} \tag{2}$$

Comparing the individual parameters, it can be seen that the relative differences of the interaction index $n$ with 4% and the convective time delay $\tau^*$ with 12% are small. But the delay time spread $\sigma^*$ is by almost 100% larger in the annular combustor when compared with the single combustor value. In the fourth column of the table, the axial coordinates of the maximum $OH^*$-chemiluminescence intensity, $X_{OH\,max}$, of the flames are given. This parameter was determined from the time averaged intensity distribution in both combustion chambers, as seen in Fig. 1. In the picture, the $OH^*$-chemiluminescense intensity is color coded ranging from white for zero intensity to black for maximum intensity. The burner exit is located on the bottom of the frame giving a side view with the flow from bottom to top. In the ACC (left picture), the location of the highest reactivity $X_{OH\,max}$ is found about 20% farther away from the burner than in the SCC (right picture). This difference is significantly larger than the comparison of time delays that would result from the same burner velocity, as they should obey the proportionality given in

$$\tau \propto \frac{X_{OH\,max}}{u_0} \tag{3}$$

Also the basic flame structures appear very different. The SCC picture on the right features a broad band of intensity with characteristic lobes at the sides, while in the ACC picture on the left, the intensity is centered in two spots on either side of the midaxis. Both findings, i.e., the missing scaling and the flame structure differences, indicate that the flow field could be very different in the annular combustor compared with the single burner case.

Contributed by the International Gas Turbine Institute of ASME for publication in the JOURNAL OF ENGINEERING FOR GAS TURBINES AND POWER. Manuscript received April 8, 2009; final manuscript received July 28, 2009; published online April 7, 2010. Editor: Dilip R. Ballal.

Table 1 Externally premixed flame parameters in the SCC and the ACC

| | $n$ | $\tau^*$ | $\sigma^*$ | $X_{OH\ max}$ $(d_0)$ |
|---|---|---|---|---|
| ACC | 3 | 1.06 | 0.57 | 0.95 |
| SCC | 3.11 | 0.93 | 0.29 | 0.76 |

With this in mind, a flow field measurement campaign and theoretical analysis was performed. The purpose was to clarify the aerodynamic effects, which govern the different flame form and position and the thermo-acoustical behavior observed in the two combustor configurations for the same operating conditions [11]. To obtain quantitative velocity data, high speed particle image velocimetry (HS-PIV) system was used to measure the velocity field in both the single and the annular combustion chambers under various conditions. In the following, we present the single and the annular test rig configurations emphasizing the experimental setup for the PIV measurements. In Sec. 3, we show the time averaged velocity maps of the EV5 burner in the single and the annular combustion chambers for the isothermal flow and for the case with combustion. Given these results, we provide a new theory based on previously reported findings that allows to anticipate the observed differences.

## 2 Experimental Setup

Figure 2 shows a view of the annular combustor test rig. Preheated air with a mass flow rate of up to 1 kg/s and a temperature up to 773 K is supplied from below, feeding into 12 fuel premixers with high pressure drop. They are used to provide externally premixed reactants to the annular plenum chamber. The annular plenum has a width of $h=136$ mm and a mean diameter of $D=437$ mm at a length of $l=223$ mm. The large area ratio between the premixers and the plenum combined with the large pressure drop provides for an acoustically hard boundary condition and thus constant equivalence ratio of the externally premixed flow. Above the plenum, the annular combustion chamber is seen. It has the dimensions $h/D/l=77$ mm/437 mm/279 mm. It is equipped with two windows to allow the observation of the flame, as well as optical access for the PIV measurement explained below. Between the plenum and the combustor, the 12 EV5 burners are mounted. At the end of the annular combustor, 12 water cooled exit nozzles provide an area contraction similar to that found in gas turbines. On six of the nozzles, phase controlled sirens are mounted, which can provide external acoustical forcing. For technical premixing, where the fuel injection is done in the burners like in the gas turbine, thus allowing equivalence ratio fluctuations, the fuel distribution can be switched from the external premixers to the burners. All flow paths were carefully equilibrated to achieve a most even distribution of fuel and air flows. In technical premixing, the rig can be operated with power ranging from 500 kW to 1600 kW and equivalence ratios of 0.5–0.67 for 573 K air preheating temperature. For external premixing at this preheating temperature, the equivalence ratio range would be 0.45–0.6. At full power and with exit nozzles, the air cooled annular combustor operates at 1 bar above ambient pressure. The PIV measurement setup is shown schematically in Fig. 3. An adaptor is mounted in place of the right window of the annular combustion chamber such that the light sheet can be introduced with little diffraction losses. The measurement plane cuts through the center of the EV5 burner at 90 deg to the slot plane. Like this, the velocity data will correspond to the meridional section of the single burner measurements.

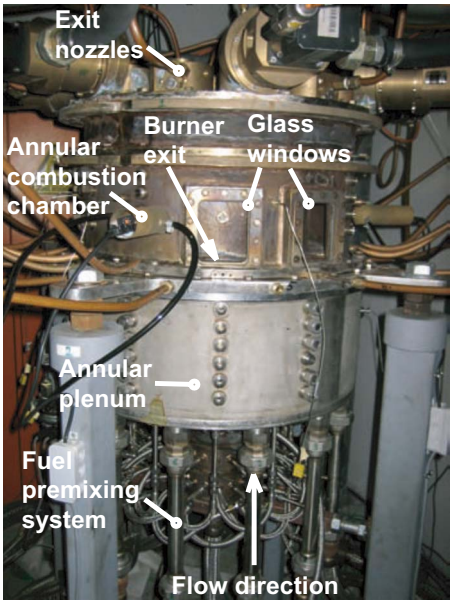


Fig. 2 ACC test rig

The SCC rig consists of an air preheater, a premixing injector for external premixing, a phase controlled siren with bypass for amplitude control, a plenum pipe, and the $90\times90$ mm$^2$ combustion chamber with a length of 700 mm. At the end, a perforated plate with carefully chosen area ratio provides a low reflection boundary condition. A close up view of the combustor can be seen in Fig. 4. Here the window adaptor used to introduce the light sheet from the top and the beam dump cavity on the bottom are shown. Figure 5 shows the schematic setup for the PIV measurement. As can be seen, the light sheet cuts through the meridional plane of the EV burner at 90 deg to the slots.

In both rigs, the high speed camera was positioned at 90 deg to the light sheet in front of the observation window. The PIV setup was completed with a seeding generator using $TiO_2$ seeding par-

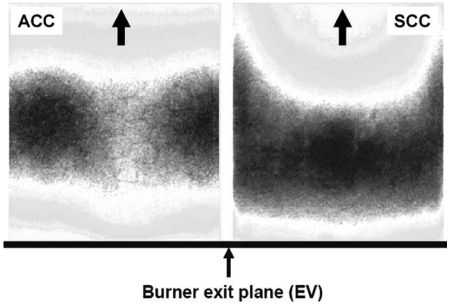


Fig. 1 OH*-chemiluminescence distribution in the annular (left) and single (right) combustion chamber with the EV burner

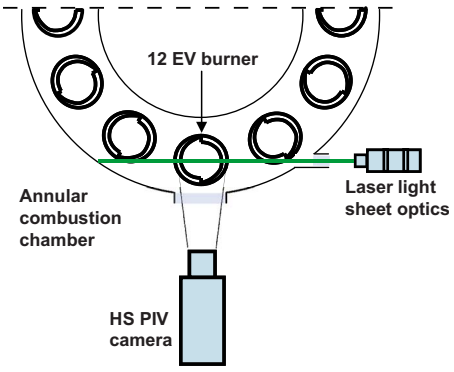


Fig. 3 Schematic of the PIV experimental setup in the ACC

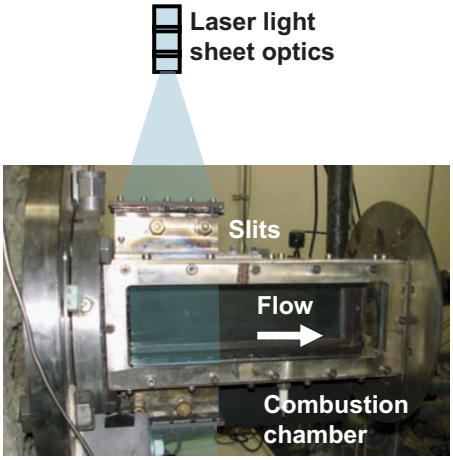


Fig. 4 SCC test rig

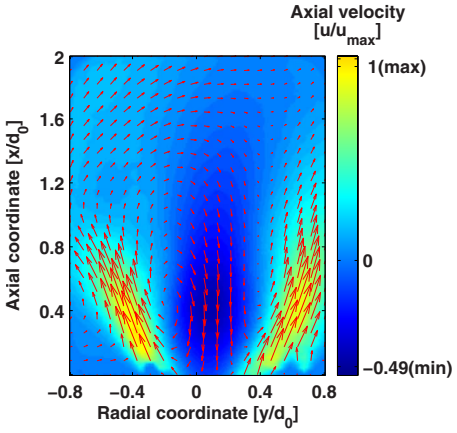


Fig. 6 PIV in the ACC without flame

ticles with a diameter of 5–10 $\mu$m as flow tracer. The high speed PIV system consists of a Nd-YAG twin laser unit with a wavelength of 532 nm. The laser is synchronized with a high speed camera equipped with a 85 mm lens and an interference filter of wavelength 532 nm ± 20 nm. The sampling frequency of the PIV system was 2000 Hz with a time delay between the laser pulses of around 20 $\mu$s. This was fine tuned according to the mean bulk velocities in the burner. A big advantage of the high sampling frequency of the PIV system was that it allowed the recording of sufficient data within a short time period before the windows got clogged with seeding particles. This aspect was of particular importance in the annular combustor where the cleaning of the windows is difficult. The postprocessing procedure of the PIV data provides two-dimensional fields of the two instantaneous planar velocity components in the combustion chamber downstream of the burner exit. From this time, averages were obtained, which are presented below. Mass balances were calculated from the isothermal flow data integrating the axial velocity profiles in the single burner test rig. The local integrals were found to be within ±15% of the metered flow rate.

## 3 Results

In the following, we present time averaged velocity fields measured in the ACC and SCC setups. In the measurements, always the same pressure drop over the EV5 burner was applied. The data for the annular combustor are shown for isothermal conditions in Figs. 6 and 8 with flame. The isothermal data for the single burner configuration are shown in Fig. 7. In all of the figures, the planar velocity vectors were plotted on the color coded field of axial velocity using the same color bar based on a fixed but undisclosed maximum velocity $u_{max}$. Thus the same color corresponds to the same axial velocity in all plots. Also the magnitude scale of the velocity vectors is the same in these figures, i.e., the same magnitude results in the same vector length. As already suspected from the flame pictures and the comparison of the delay times with the $X_{OH\ max}$ mentioned in the Introduction, a large difference in the flow field can be observed between the two configurations.

In the annular combustor data shown in Fig. 6, a typical swirling jet flow with about 30 deg jet half angle is seen with an inner recirculation zone (IRZ) of $0.5d_0$ width and $1.5d_0$ length. The inner recirculation axial velocity is about half the peak jet velocity, which together with the IRZ width results in about 15% recirculation rate that is common for this kind of flow. Inspecting the outer jet boundary, the velocity vectors show a pattern very similar to free jet flow. A slight asymmetry is seen in that the recirculation bubble and the jet lobes are tilted to the right. Considering the swirl direction of the burners (see Fig. 3) and the induced azimuthal secondary flows in the annulus, which are clockwise at the inner diameter and counterclockwise at the outer diameter of the annulus, this seems to indicate that the burner midplane does not coincide with the zero velocity surface separating the inner and outer azimuthal secondary flows.

The flow field of the single combustor plotted in Fig. 7 is rather different. For the same swirl number ($\vartheta_{eff}=1$), the jet half angle is increased to 50 deg and the IRZ width has grown to almost $0.8d_0$. The axial velocity in the IRZ has increased such that almost twice the recirculation rate of the annular combustor case results. The forward axial velocity has only 70% of the magnitude of the an-

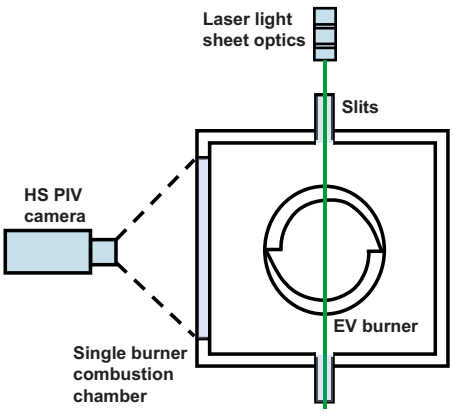


Fig. 5 Schematic of the PIV experimental setup in the SCC

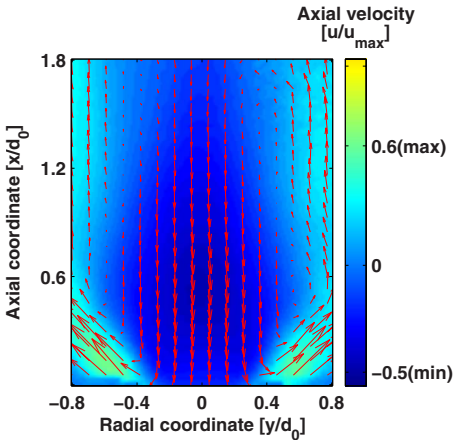


Fig. 7 PIV in the SCC without flame

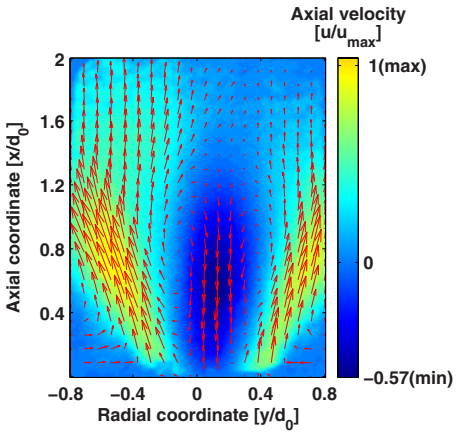


Fig. 8 PIV in the annular combustor with flame

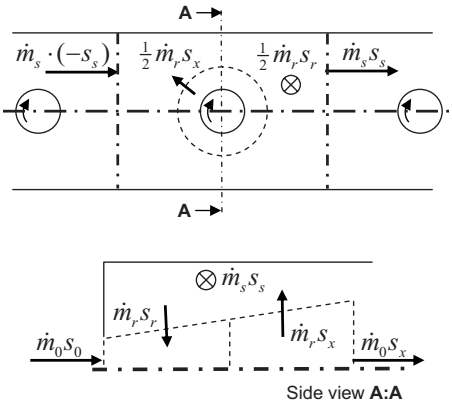


Fig. 9 Schematic of jet swirl balance

nular combustor, which explains why the delay times given in Table 1 are quite similar in spite of the large difference in $X_{\mathrm{OH\ max}}$ and the flame shape. Due to limitation of the window size in the single burner combustor, the outer jet boundary could not be fully resolved.

Summarizing the comparison of the isothermal velocity fields between annular and single burner combustors, it can be stated that two very different flow fields are found, which in this case form a rather questionable basis for using the dynamic flame data of the single burner flame for the analysis of the annular combustor.

Figure 8 presents the flow field for the case with flame in the annular combustor. The air mass flow was kept the same as in the isothermal case (Fig. 6). The effect of volume expansion due to the heat input in the reaction zone can be recognized especially in the longer jet, stretching up to $1.3d_0$, whereas in the cold case, it reaches only $0.9d_0$. However, the basic structure remains the same as in the isothermal case.

**3.1 Critical Confinement Scaling.** The change in the flow field between the single burner rig and the annular combustor was investigated further based on the findings recently presented by Fu et al. [14]. Fu et al. [14] demonstrated two flow regimes of a swirling jet entering into a square combustion chamber. The *wall jet regime* where the swirling jet spreads quickly and high axial velocities are seen close to the combustor walls and the *free jet regime* where the flow field resembles that of a swirling jet issuing into quiescent ambient. The occurrence of either regime depended on the degree of confinement seen by the swirling jet, i.e., the area ratio between the swirler exit and combustor. For a given swirler having an effective swirl number $\vartheta_{\mathrm{eff}}=0.45$ as calculated from Eq. (10) below, Fu et al. [14] found that the transition between the regimes took place at an area ratio of $A_{cc}/A_{bu}=5.88$.

As seen in Fig. 7, the flow field in the single combustor with the EV5 burner shows the wall jet regime, whereas the flow structure in the annular combustor, Fig. 6, has the free jet type. Since the area ratio between combustor and burner is almost the same[1] for both cases, a fundamental difference must be occurring. The obvious differences between the two systems are the missing side walls in the case of the annular rig, which are giving rise to mass flow along the circumference and also to a change in the radial pressure field for the burner jet flow. The overall entrainment mass balance of the individual jet in either system should be similar due to the periodic symmetry. But the missing side walls in the annular combustor change the angular momentum balance for the jet considered. In the ACC, the entrainment mass flow will carry much less angular momentum because it stems also from the neighboring burners. As discussed in the Appendix, these have opposite swirl with respect to the axis of the jet considered, which reduces the entrained angular momentum flux and in turn reduces the centrifugal force acting on the jet. In contrast to this, the mass flow recirculating in the outer recirculation zone of the single burner combustor returns the angular momentum, such that the decrease in swirl velocity due to entrainment will be considerably smaller than in the free jet. Therefore, the centrifugal force driving the jet flow outward will be preserved longer, extending the jet core region. If the combustor diameter is large enough, such that the negative axial velocities associated with the outer recirculation are small, the axial pressure gradient needed to drive them is also small. In this case, the swirling jet flow development, e.g., its expansion angle, is dominated by the balance of inertia [15]. If the combustor cross section area is decreased, the recirculation velocities and the associated axial pressure gradient rise until at the critical confinement the jet angle suddenly increases significantly. Now the jet touches the combustor wall and effectively blocks recirculation from downstream. The inertia associated with the increased jet angle balances the axial pressure gradient caused by entrainment flow and the new force balance creates the wall jet regime. While the details of this process may be even more involved, we argue below that the critical area ratio will scale with the entrainment mass flow rate of the swirling jet, since the ratio of both provides for the recirculation velocity and thus for the axial pressure gradient.

To obtain a functional description of the angular momentum transferred with the outer recirculation of the jet, we consider the following crude balance of angular momentum. The ansatz used for this is analogous to a stirred vessel balance of, e.g., enthalpy fluxes and uses concepts, as proposed in the book by Panton [16]. Control volumes are defined to which fluxes of angular momentum can be formulated. These mix within the volumes, thus creating new "concentrations" of angular momentum $s_i$, which are then carried out across the boundaries. We define the mass specific mean angular momentum $s_i$ $(\mathrm{m}^2/\mathrm{s})$ as

$$s_i \equiv \frac{\int_{(\dot{m}_i)} w_i \cdot r_i \cdot d\dot{m}_i}{\dot{m}_i} \tag{4}$$

In Eq. (4), the numerator on the right hand side is the flux of angular momentum with mass flow rate $\dot{m}_i$. In Fig. 9, the upper half shows a schematic view of the front panel of the annular combustor from downstream. Half of the cut through the middle jet is drawn below. There are three neighboring swirlers with a clockwise swirl orientation. The swirling flow induces the formation of circumferential mass flow rates $\dot{m}_s$, which flow to the right on the top half and to the left on the bottom half of the annulus. The jet flow enters into the combustor with the mass flow rate of $\dot{m}_0$. Due to jet entrainment, the recirculation mass flow rate $\dot{m}_r$ forms.

[1] 1/12 of the ACC area is about 8% larger than the SCC area.

Considering the side view first, we can set up a balance of angular momentum flux by assuming the mixing of jet and recirculation flux.

$$\dot{m}_0 s_0 + \dot{m}_r s_r - (\dot{m}_0 + \dot{m}_r) s_x = 0 \tag{5}$$

Here $s_0$ is the specific angular momentum the swirler provides, $s_r$ is the value that is entrained from the recirculation zone, and $s_x$ is the specific angular momentum that the jet provides to the outer recirculation zone and further downstream. Considering just the top half now, the flux of angular momentum from the jet to the outer recirculation, $1/2\dot{m}_r s_x$, is mixed with the flux from the side $-\dot{m}_s s_s$. Here the minus sign signifies that the burner to the left has the opposite specific swirl, as shown in the Appendix. The mixture has the specific angular momentum $s_s$ and leaves in part $\dot{m}_s s_s$ over the right side to the next burner, as well as upstream to be entrained by the jet $1/2\dot{m}_r s_r$. Clearly the magnitude of $s_s$ will change along the distance from the burner nozzle. At the end of the jet, we expect $s_s = s_x$, while at the root, it would be $s_s = s_r$. Assuming a linear profile, we can write $s_s = 0.5(s_r + s_x)$. With this, the balance equation for the outer recirculation volume becomes

$$-\dot{m}_s \cdot \tfrac{1}{2}(s_r + s_x) + \tfrac{1}{2}\dot{m}_r s_x - \dot{m}_s \cdot \tfrac{1}{2}(s_r + s_x) - \tfrac{1}{2}\dot{m}_r s_r = 0 \tag{6}$$

Combining Eqs. (5) and (6), we can eliminate $s_x$ and solve for the specific angular momentum entrained by the jet.

$$s_r = \frac{s_0\left(1 - 2\dfrac{\dot{m}_s}{\dot{m}_r}\right)}{1 + 2\dfrac{\dot{m}_s}{\dot{m}_r} + 4\dfrac{\dot{m}_s}{\dot{m}_0}} \tag{7}$$

From Eq. (7), the effect of the side flow can be seen. For vanishing side flow $\dot{m}_s = 0$, the recirculating flow has the same specific angular momentum as the nozzle flow. With increasing side flow, the returning angular momentum will become smaller.

To draw more quantitative conclusions, the mass flow rates of side and entrainment flow need to be known. To obtain an estimate for the side mass flow rate, we can approximate the induced velocities on the side planes from point vortex theory and integrate them. As shown in the Appendix, this gives the following relation, where the constant was fixed using the data from an earlier publication [18]:

$$\dot{m}_s \approx 0.28 \cdot \left(\frac{A_{cc}}{A_{bu}}\right)^{0.5} \cdot \vartheta_{\text{eff}} \cdot \dot{m}_0 \tag{8}$$

An estimate for the entrainment mass flow rate $\dot{m}_r$ of a swirling jet is obtained from the work of Meier [19] who investigated isothermal free swirling jets. He derived the following entrainment correlation from his experiments:

$$\frac{\dot{m}_x}{\dot{m}_0} = \left(0.32\frac{x}{d_0} + 4.4\,\vartheta_{\text{eff}}\right) \tag{9}$$

Here $\dot{m}_x$ is the total mass flow rate at some position $x/d_0$ downstream of the swirler and $\dot{m}_0$ is the swirler mass flow rate. The nondimensional effective swirl number of the jet $\vartheta_{\text{eff}}$ in Eq. (9) is defined by

$$\vartheta_{\text{eff}} = \frac{\int_{(\dot{m})} w \cdot r \cdot d\dot{m}}{\int_{(\dot{m})} u \cdot d\dot{m} \cdot R_{\text{eff}}}$$

$$R_{\text{eff}} = \frac{1}{\dot{m}} \cdot \int_{(\dot{m})} r \cdot d\dot{m} \tag{10}$$

Equation (9) reflects the experimental finding that the additional entrainment due to swirl is restricted to the burner near field, while downstream the jet flow continues like a free nonswirling jet. From Meier's data [19], also the length of this core region of the jet in dependence of the swirl number can be obtained. Here it was correlated in the following way that also provides the well known $10d_0$ core distance of the nonswirling turbulent round jet for $\vartheta_{\text{eff}} = 0.0$.

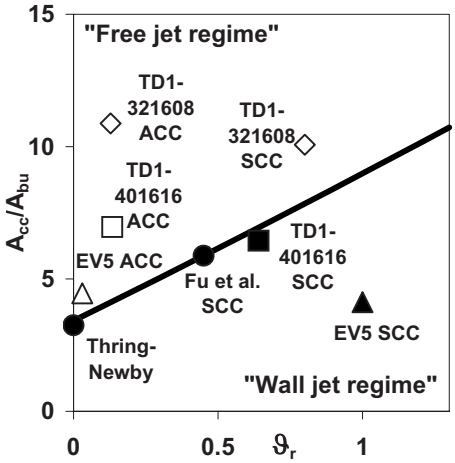


**Fig. 10 Comparison of confinement theory Eq. (13) with experimental data from various burners in the SCC and ACC, as well as from previous axial jet theory [17]**

$$\frac{x_m}{d_0} = 10 \cdot \exp(-0.3 \cdot \vartheta_{\text{eff}}) \tag{11}$$

Comparing the specific axial momentum fluxes of forward jet $u_0^2$ and outer recirculation flow $u_r^2$, we propose that for a given critical ratio the transition between free and wall jet regime occurs.

$$\left(\frac{u_0^2}{u_r^2}\right)_{\text{crit}} = \left(\frac{\dot{m}_0}{\dot{m}_r} \cdot \frac{A_{cc}}{A_{bu}}\right)^2$$

$$\left(\frac{A_{cc}}{A_{bu}}\right)_{\text{crit}} = C_{\text{crit}} \cdot \frac{\dot{m}_r}{\dot{m}_0} \tag{12}$$

With $\dot{m}_r = \dot{m}_{x_m} - \dot{m}_0$ to obtain the recirculation mass flow rate from Meier's correlation by inserting $\vartheta_{\text{eff}} = 0.45$ into Eqs. (9) and (11) and setting $A_{cc}/A_{bu} = 5.88$ as determined by Fu et al. [14], we can fix the constant $C_{\text{crit}} = 1.56$. So finally the model reads

$$\left(\frac{A_{cc}}{A_{bu}}\right)_{\text{crit}} = 1.56 \cdot \left(0.32\frac{x_m}{d_0} + 4.4\,\vartheta_{\text{eff}} - 1\right) \tag{13}$$

In Fig. 10, this model is shown as a solid line together with data points from our experimental testing. The solid symbols refer to cases in the wall jet regime, while the hollow symbols indicate free jet behavior. In the graph, the ordinate is the effective area ratio from the combustor (sector) to the burner and on the abscissa the effective swirl number of the recirculation $\vartheta_r$ is given. Using Eqs. (7) and (8), it is calculated from $s_r$ as

$$\vartheta_r = \frac{\dot{m}_0 \cdot s_r}{\int_{(\dot{m})} u \cdot d\dot{m} \cdot R_{\text{eff}}} = \vartheta_{\text{eff}} \frac{s_r}{s_0} \tag{14}$$

In order to estimate the recirculation mass flow rate, Eq. (13) can be rearranged.

$$\frac{\dot{m}_r}{\dot{m}_0} = 0.64 \cdot \left(\frac{A_{cc}}{A_{bu}}\right)_{\text{eff}} \tag{15}$$

As shown above in Eq. (7), the swirl number for the SCCs is that of the burner, whereas in the ACC it is reduced. The EV5 burner SCC data point can be seen well within the wall jet regime, which is confirmed from Fig. 7. For the ACC case, the estimated swirl number $\vartheta_r$ moves the EV5 ACC data point just into the free jet regime, which is in accordance to our experimental finding (Fig. 6).

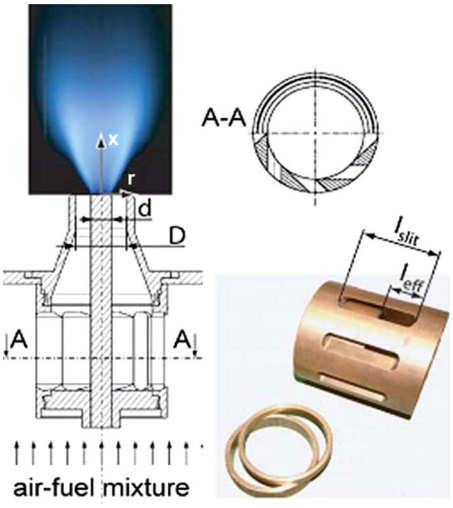


**Fig. 11 Schematic of the TD1 burner**

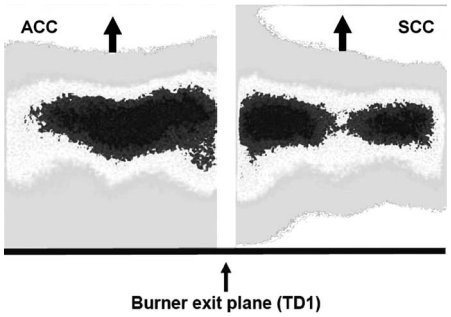


**Fig. 12 OH*-chemiluminescence distribution in the annular (left) and single (right) combustion chamber with the TD1-321608 burner**

Further data obtained for the generic "TD1-xxyyzz"[2] burner shown in Fig. 11 support this theory for different geometry parameters. For the TD1-401616 burner, the theory predicts that transition between the flow regimes occurs, which was also observed experimentally. The TD1-321608 burner should, according to theory, be in the free jet regime both in the SCC and the ACC. Thus similar flame geometries are expected. This is confirmed in Fig. 12 where almost identical flame structures are observed in the single and the annular combustor.

Finally, the result from the classical theory by Thring and Newby [17] for axial nonswirling jets is also given in Fig. 10. It coincides very well with the $\vartheta_{\text{eff}}=0$ value of this independent scaling law, which gives further confidence in our analysis.

## 4 Summary and Conclusions

An experimental investigation of the flow field of an annular combustor and a single burner combustor with the same burner was performed. It has revealed the aerodynamic effect, which causes the discrepancies in the flame transfer function behavior measured at the same operating conditions in the single and the annular combustion chambers. The results have shown significant differences in the flow field. In particular, it was seen that for the investigated system in the annular combustor a free swirling jet flow forms, while in the single burner configuration a swirling wall jet flow regime exists.

[2] *xx* encodes the nozzle diameter *D*, *yy* encodes the center body diameter *d*, and *zz* encodes the swirler slot length $l_{\text{eff}}$, all in mm,

For a fixed single swirler configuration, such behavior had been reported earlier [14]. There it was observed that the area ratio between combustor and burner in the single burner combustion chamber had a critical value where for a given swirler the flow regimes switched. In this paper, we discuss the physical mechanism and show how to generalize the earlier finding. We propose a new correlation, which serves to estimate this critical value for other swirl combustor geometries. It explains the observed change in the flow field between single burner and annular combustor for the EV5 burner. The new theory also works well with the experimental data from other burner geometries and holds in comparison with previous independent literature for confined nonswirling jet flow.

Given the area ratio between combustor sector cross section and burner area and the operation temperatures, the theory allows to estimate the swirling jet flow regime for coswirling burners in an annular combustion chamber. With this information, single burner experiments, to obtain the flame transfer function, can be designed with respect to choosing the area ratio in the SCC test rig in order to best reproduce the ACC flow regime.

In conclusion, we state that the measurement of dynamic flame parameters in a single burner test rig to be used in the stability analysis of an annular combustor requires a careful choice of the single burner combustor dimensions to obtain similar flames. The theory and concepts developed here should help to achieve this goal.

## Acknowledgment

This project was funded by Alstom, Bayerische Forschungsstiftung, Bayerisches Staatsministerium für Wirtschaft, Forschung und Kunst, and Bayerisches Staatsministerium für Wirtschaft, Infrastruktur und Technologie in the framework of KW21. Their support is gratefully acknowledged.

## Nomenclature

$A$ = cross-sectional area ($m^2$)
$d, D$ = diameter (m)
$\dot{D}$ = flux of angular momentum (N m)
$h$ = ACC width, SCC side length (m)
$\dot{I}$ = flux of axial momentum (N)
$\dot{m}$ = mass flow rate (kg/s)
$n$ = interaction index
$r, R$ = radius (m)
$\vartheta$ = swirl number
$s_i$ = specific angular momentum of flux $i$ ($m^2/s$)
$u, v, w$ = axial, radial, and tangential velocities (m/s)
$x$ = axial coordinate (m)
$X_{\text{OH max}}$ = axial coordinate of OH* maximum (m)
$y, r$ = radial coordinate (m)
$\tau^*$ = normalized convective time delay
$\sigma^*$ = normalized time delay variance
bu = burner
cc = combustion chamber
eff = effective
$m$ = core region coordinate
$r$ = recirc. mass flow, entr. spec. ang. mom.
$s$ = circumferential side mass flow
$x$ = downstream ejected spec. ang. mom.
0 = nominal burner quantity

## Appendix

We consider the dependence of the side mass flow $\dot{m}_s$ in the annular combustor on the mass flow rate and the swirl strength of the burners for the coswirling arrangement.

In Figs. 13(*a*) and 13(*b*), the kinematics of the flow field at the interface between two burners are shown. We assume that the burners can be described as two corotating ideal vortices with

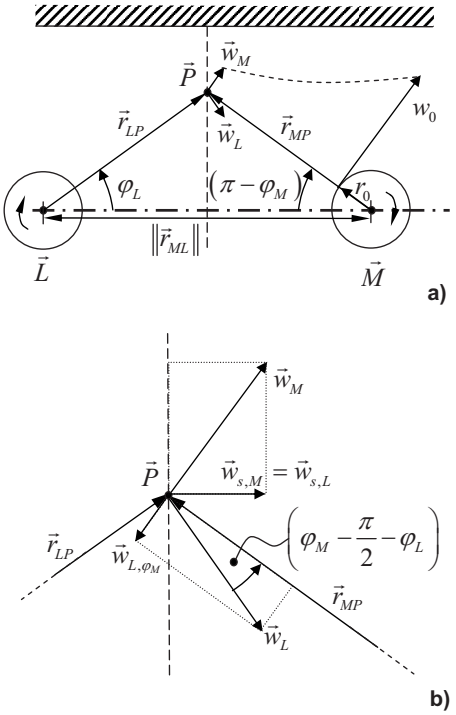


**Fig. 13 Schematic flow field kinematics for a point *P* on the interface between two burners at *M* and *L*. (*a*) Global situation. (*b*) Detail at point *P*.**

circulation $w_0 r_0$ located at the points ***L*** and ***M***. ***M*** represents the burner considered in the swirl balance equations (5) and (6). At a point ***P*** on the interface, the velocities $\boldsymbol{w}_L$ and $\boldsymbol{w}_M$ are induced. Projecting $\boldsymbol{w}_L$ into the $\boldsymbol{M}, \varphi_M$ coordinate system, as shown in Fig. 13(*b*), we get the swirl velocity component $\boldsymbol{w}_{L,\varphi_M}$, which is obviously negative compared with $\boldsymbol{w}_M$. The specific angular momentum of the *L*-velocity with respect to the *M*-burner at point ***P*** is calculated as

$$\begin{aligned} s_{L,M}(\boldsymbol{P}) &= \boldsymbol{w}_L \times \boldsymbol{r}_{MP} \\ &= -\frac{w_0 r_0}{\|r_{LP}\|} \cdot \sin\left(\varphi_M - \varphi_L - \frac{\pi}{2}\right) \cdot \|r_{MP}\| \cdot \boldsymbol{e}_x \\ &= -w_0 r_0 \sin\left(2\varphi_M - \frac{3\pi}{2}\right) \cdot \boldsymbol{e}_x \end{aligned} \tag{A1}$$

Here $\boldsymbol{e}_x$ is the unit vector in the axial direction of the burner/combustor. The induced velocity $u_s$ at point ***P*** normal to the interface is obtained from Fig. 13(*b*) as

$$\begin{aligned} u_s(\boldsymbol{P}) &= \|w_L\| \cdot \cos\left(\frac{\pi}{2} - \varphi_L\right) + \|w_M\| \cdot \cos\left(\varphi_M - \frac{\pi}{2}\right) \\ &= 4 \cdot \frac{w_0 r_0}{\|r_{ML}\|} \cdot \cos^2\left(\varphi_M - \frac{\pi}{2}\right) \end{aligned} \tag{A2}$$

With this relation, we can estimate the side mass flow rate $\dot{m}_s$ per unit axial length of the combustor.

$$\frac{\dot{m}_s}{\rho \cdot l} = \int_{\varphi_1}^{\pi} u_s \cdot \|r_{MP}\| \cdot \cos(\pi - \varphi_M) d\varphi = \text{const} \cdot w_0 r_0 \tag{A3}$$

Here $\varphi_1 = \pi - \arctan(h/\|r_{ML}\|)$, where $h$ is the ACC width. Using the specific angular momentum definition (Eq. (4)) and the definition of swirl number (Eq. (10)), we get

$$w_0 r_0 = \frac{\dot{D}_0}{\dot{m}_0} = \frac{\dot{I}_0 \cdot R_{\text{eff}} \cdot \vartheta_{\text{eff}}}{\dot{m}_0} = \text{const} \cdot \frac{\dot{m}_0^2 \cdot R_{\text{eff}}}{\rho A_{bu} \cdot \dot{m}_0} \cdot \vartheta_{\text{eff}} \tag{A4}$$

Inserting this into Eq. (A3), solving for $\dot{m}_s$, and simplifying ($R_{\text{eff}} \approx \text{const} \cdot \sqrt{A_{bu}}$, $l \approx \text{const} \cdot \sqrt{A_{cc}}$), Eq. (8) is obtained.

## References


[1] Sattelmayer, T., and Polifke, W., 2003, "Assessment of Methods for the Computation of the Linear Stability of Combustors," Combust. Sci. Technol., **175**(3), pp. 453–476.

[2] Sattelmayer, T., and Polifke, W., 2003, "A Novel Method for the Computation of the Linear Stability of Combustors," Combust. Sci. Technol., **175**(3), pp. 477–497.

[3] Schuermans, B., Bellucci, V., and Paschereit, C. O., 2003, "Thermoacoustic Modeling and Control of Multi Burner Combustion Systems," ASME Paper No. GT2003-38688.

[4] Schuermans, B. B. H., Polifke, W., and Paschereit, C. O., 1999, "Modeling Transfer Matrices of Premixed Flames and Comparison With Experimental Results," ASME Paper No. 99-GT-132.

[5] Polifke, W., and Paschereit, C., 1997, "Characterization of Lean Premixed Gas Turbine Burners as Acoustical Multi-Ports," APS/DFD Annual Meeting, San Francisco, CA.

[6] Abom, M., 1986, "A Note on Random Errors in Frequency Response Estimators," J. Sound Vib., **107**, pp. 355–358.

[7] Munjal, M. L., and Doige, A. G., 1990, "Theory of a Two Source-Location Method for Direct Experimental Evaluation of the Four-Pole Parameters of an Aeroacoustic Element," J. Sound Vib., **141**, pp. 323–333.

[8] Schuermans, B. B. H., Polifke, W., Paschereit, C. O., and van der Linden, J. H., 2000, "Prediction of Acoustic Pressure Spectra in Combustion Systems Using Swirl Stabilized Gas Turbine Burners," ASME Paper No. 2000-GT-0105.

[9] Schuermans, B., Luebcke, H., Bajusz, D., and Flohr, P., 2005, "Thermoacoustic Analysis of Gas Turbine Combustion Systems Using Unsteady CFD," ASME Paper No. GT2005-68393.

[10] Krebs, W., Prade, B., Flohr, P., and Hoffmann, S., 2002, "Thermoacoustic Stability Chart for High-Intensity Gas Turbine Combustion Systems," Combust. Sci. Technol., **30**, pp. 99–128.

[11] Fanaca, D., Alemela, P. R., Ettner, F., Hirsch, C., Sattelmayer, T., and Schuermans, B., 2008, "Determination and Comparison of the Dynamic Characteristics of a Perfectly Premixed Flame in Both Single and Annular Combustion Chambers," ASME Paper No. GT2008-50781.

[12] Alemela, P. R., Fanaca, D., Ettner, F., Hirsch, C., Sattelmayer, T., and Schuermans, B., 2008, "Flame Transfer Matrices of a Premixed Flame and a Global Check With Modelling and Experiments," ASME Paper No. GT2008-50111.

[13] Schuermans, B., Bellucci, V., Guethe, F., Meili, F., Flohr, P., and Paschereit, O., 2004, "A Detailed Analysis of Thermoacoustic Interaction Mechanisms in a Turbulent Premixed Flame," ASME Paper No. GT2004-53831.

[14] Fu, Y., Cai, J., Jeng, S.-M., and Mongia, H., 2005, "Confinement Effects on the Swirling Flow of a Counter-Rotating Swirl Cup," ASME Paper No. GT2005-68622.

[15] Hirsch, C., Fanaca, D., Reddy, P., Polifke, W., and Sattelmayer, T., 2005, "Influence of the Swirler Design on the Flame Transfer Function of Premixed Flames," ASME Paper No. GT2005-68195.

[16] Panton, R. L., 1984, *Incompressible Flow*, Wiley, New York.

[17] Thring, M., and Newby, M., 1953, "Combustion Length of Enclosed Turbulent Jet Flames," Fourth International Symposium on Combustion, Baltimore, MD, pp. 789–796.

[18] Hirsch, C., Kuenzi, T., Knopfel, H., Paikert, B., Steinbach, C., Geng, W., and Döbbeling, K., 2002, "An Annular Combustor Natural Gas Ignition Model Derived From Atmospheric Sector Experiments," ASME Paper GT-2002-30073.

[19] Maier, P., 1968, "Untersuchung isothermer drallbehafteter Freistrahlen," Forsch. Ingenieurwes., **34**(5), pp. 133–140.